

Title:

**A time dependent micro-mechanical fiber
composite model for inelastic zone growth in
viscoelastic matrices**

Author(s):

I.J. Beyerlein, C.H. Zhou, L.S. Schadler

Submitted to:

<http://lib-www.lanl.gov/cgi-bin/getfile?00937075.pdf>



A time dependent micro-mechanical fiber composite model for inelastic zone growth in viscoelastic matrices

I.J. Beyerlein ^{a,*}, C.H. Zhou ^b, L.S. Schadler ^b

^a *Theoretical Division, Los Alamos National Laboratory, Mail Stop B216, Los Alamos, NM 87545, USA*

^b *Materials Science and Engineering, Rensselaer Polytechnic Institute, Troy, NY 12180, USA*

Received 15 March 2002; received in revised form 10 December 2002

Abstract

In this work, a fiber composite model is developed to predict the time dependent stress transfer behavior due to fiber fractures, as driven by the viscoelastic behavior of the polymer matrix, and the initiation and propagation of inelastic zones. We validate this model using in situ, room temperature, micro-Raman spectroscopy fiber strain measurements. Multifiber composites were placed under constant load creep tests and the fiber strains were evaluated with time after one fiber break occurred. These composite specimens ranged in fiber volume fraction and strain level. Comparison between prediction and MRS measurements allows us to characterize key in situ material parameters, the critical matrix shear strain for inelastic zones and interfacial frictional slip shear stress. We find that the inelastic zone is predominately either shear yielding or interfacial slipping, and the type depends on the local fiber spacing.

© 2003 Elsevier Science Ltd. All rights reserved.

Keywords: Fracture; Polymer matrix composites; Creep; Micro-Raman spectroscopy; Interfacial slipping; Plastic matrix

1. Introduction

Under steady loads, polymer matrix fiber composites will fail in creep rupture, even at room temperature (Brinson et al., 1981; Brinson and Dillard, 1982; Shanghnessy and Snide, 1984; Phoenix et al., 1988), while accompanied with little to no macroscopic creep. At the micro-scale, however, damage nucleates and grows in time after the application of load. This time dependent failure process primarily begins when the effects of matrix creep relaxation and defects interact. Both the stress state and evolution of the stress state can change as a result of such interactions, promoting delayed fiber breaks and inelastic zone growth (Lifshitz and Rotem, 1970; Otani et al., 1991; Iyengar and Curtin, 1997; Beyerlein, 2000).

Inelastic zones can initiate and grow from fiber breaks to an extent observable by eye (Zhou et al., 2002; Miyake et al., 1998). Visible inelastic zones are most likely ‘slip’ zones, where the interface has failed, but they can also consist partially of an irreversible ‘plastic’ zone, in which the polymer matrix has irreversibly

* Corresponding author. Tel.: +1-505-665-2231; fax: +1-505-665-5926.

E-mail address: irene@lanl.gov (I.J. Beyerlein).

Nomenclature

A	$A = \pi r^2$, fiber cross-sectional area
α	exponent in the power law functions for polymer creep
d	diameter of the fiber
E	Young's modulus of the fiber
$\varepsilon(x, t)$	fiber axial strain as a function of time and distance from the fiber break
$\varepsilon^*(t)$	applied far field fiber strain
$\varepsilon_r(t)$	residual compressive strain at the fiber break end
γ	matrix shear strain
γ_c	critical matrix shear strain to initiate slipping or matrix yielding
$J(t)$	time dependent shear compliance for the polymer
J_0	generic elastic compliance constant, either J_c or J_e
J_c	elastic compliance constant in the complete power law function
J_e	elastic compliance constant in the incomplete power law function
$l(t)$	inelastic zone length
$L_r(t)$	load recovery length
$A_r(t)$	normalized load recovery length
r	radial distance from the fiber center
r_0	radius of the fiber
t	normalized time
\mathcal{T}	real time
\mathcal{T}_c	characteristic time in the power law functions for matrix creep
τ_d	interfacial shear stress in the inelastic zone
$\tau_r(r, x)$	shear stress as a function of radial distance from the fiber
$\tau_i(x, t)$	interfacial shear stress
τ_{\max}	maximum interfacial shear stress
τ_0	normalized interfacial shear stress for inelastic zones
τ^*	normalized interfacial shear stress for viscoelastic matrix
$U(x, t)$	differential displacement between the fiber and the matrix
$V(x, t)$	fiber displacement
u_c	critical displacement between the fiber and the matrix
w	surface to surface fiber spacing in the model composite
w'	effective surface to surface fiber spacing in the model composite
x	fiber axial coordinate
Ψ_F	fraction of far field fiber strain used in another criterion for $L_r(t)$
Ψ_i	fraction of maximum stress shear used in our criterion for $L_r(t)$

sheared yet is still bonded to the fiber (Gulino et al., 1991; Beyerlein et al., 1998b). Under quasi-static conditions, inelastic zones are assumed to initiate and grow under a critical shear stress, which causes irreversible stretching of the polymer network. The yield shear stress and frictional stress that remain after initiation and exist within the zones, τ_d however will be lower than this critical value. Typically, the value of the frictional shear force depends on the interface roughness, contraction forces due to cure shrinkage of the matrix, and Poisson's ratio effects (Schadler and Galiotis, 1995; Melanitis et al., 1993). Under steady load creep conditions wherein matrix stress relaxation decreases interfacial shear stresses, in time inelastic zones are still found to initiate and grow (Zhou et al., 2002).

Fiber volume fraction V_f (or inversely fiber spacing w) can play a role in determining the type of inelastic zone (Beaumont and Phillips, 1967; Gulino et al., 1991; Beyerlein and Phoenix, 1997), apart from material system and fiber surface treatments. In low V_f composites, the interface slips, whereas in large V_f composites, the matrix tends to yield. Such a transition is likely attributed to transitions in the stress state or material behavior or both. As an example, consider the epoxy matrix material studied here which is brittle and linear elastic to failure in bulk form. Yet as a thin film (few microns thick), epoxy has a nonlinear ductile-like response, which can withstand larger strains prior to failure (Glad, 1986) than in bulk. Consequently in low V_f composites, interfacial failure is expected over ductile-like matrix behavior. However as V_f increases or equivalently as w approaches a few microns or the submicron range, the epoxy matrix in between may begin to behave as a thin film (Gulino et al., 1991) and ductile-like behavior will be favored over interfacial failure. Nonetheless the possibility of a difference between the bulk and thin film matrix behavior renders the matrix in situ behavior an unknown.

Micro-Raman spectroscopy (MRS) can be used to study the in situ fiber strains and matrix stresses around fiber breaks in high modulus fiber composites with transparent matrices (Schadler and Galiotis, 1995). Fig. 1 shows a typical fiber strain (circles) distribution in x , axial fiber coordinate, along a broken fiber obtained via MRS. Also shown is one possible interfacial shear stress profile $\tau_i(x)$ (squares), which satisfies equilibrium, that one can determined from the MRS fiber strain data, all at a fixed time t . (The symbols are data and a curve is drawn through them to guide the eye.)

One can obtain much information from plots like Fig. 1. In the inelastic region, the fiber strain increases linearly from the fiber break at $x = 0$ and the interfacial shear stress $\tau_i(x)$ is a constant τ_d . The distance between the fiber break and the peak value of $\tau_i(x)$, τ_{\max} , is defined as the inelastic length, $l(t)$. Outside the inelastic region, the fiber axial strain increases nonlinearly until it reaches the applied axial strain ε^* and $\tau_i(x)$ gradually decreases from τ_{\max} to zero. The load recovery length, $L_r(t)$, is defined as the distance in x between $l(t)$ and the point where τ_i decays to a small fraction Ψ_i of τ_{\max} .

Naturally as the matrix stiffness changes due to creep, the stress distributions produced by the fiber fracture will change as well. Therefore, MRS measurements of fiber strain in time can, in principle, lead to information on the time change of matrix and interface properties and inelastic zones. Only recently has MRS been used to make fiber strain measurements in composites under creep conditions: a single short fiber composite (Thomsen and Pryz, 1999; Schjødt-Thomsen and Pryz, 2000), a single fiber composite

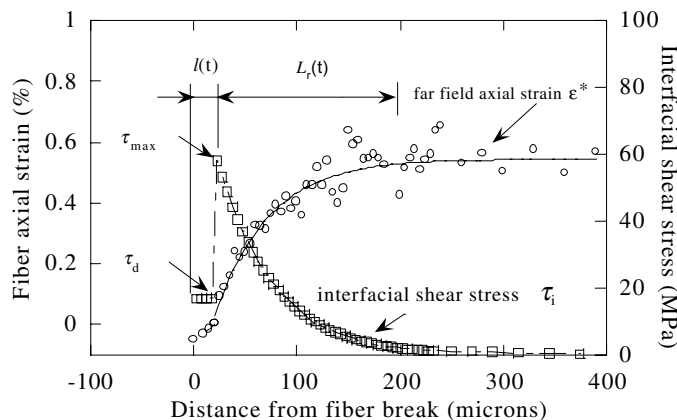


Fig. 1. Typical MRS measurements for the axial fiber strain and interfacial shear stress profiles from the fiber break within composite specimens and definitions of the far field strain ε^* , inelastic zone $l(t)$, load recovery length $L_r(t)$, peak interfacial shear stress τ_{\max} and inelastic zone stress τ_d .

(Miyake et al., 1998), and multifiber composites (Zhou et al., 2002). In these works, inelastic interface and matrix behavior were detected, though the interpretative models used assumed perfect fiber-matrix bonding.

Despite this discrepancy, our analysis of multifiber composite specimens (Zhou et al., 2002), did provide useful results for much of the present work. In this prior work, we applied two models, a single and multifiber shear lag model to interpret the time dependent fiber strain data generated by isolated fiber breaks. Both models assumed a perfect interface and a viscoelastic matrix that deforms only in shear. We first demonstrated the similarity between the in situ versus ex situ creep responses of the matrix at room temperature, an assumption we will retain in the present study. Secondly, we found that for composites which had rather large fiber spacings (≈ 5 – 7 fiber diameters), both the single and multifiber models performed well. Thirdly we found that $L_r(t)$ increased with the square root of the matrix compliance and τ_{\max} decreased inversely with the square root of the matrix compliance, in agreement with several analytical stress transfer models for viscoelastic matrix composites (Lifshitz and Rotem, 1970; Ohno and Miyake, 1999; Lagoudas et al., 1989; Beyerlein et al., 1998a). Such impressive agreement occurred only at short times and low applied stresses when the inelastic zones were small or negligible. Discrepancies between MRS data and these two viscoelastic models elucidated that inelastic zones tend to increase the time rate of change of the fiber strain profile over that of viscoelastic behavior. Therefore it was quite clear that these models needed to be extended to include a combination of inelastic zones and matrix creep at this length scale ($<$ fiber diameter). This paper is concerned with developing such a model.

In this work, several samples varying in V_f and strain level were tested in creep conditions and the time dependent strains were mapped along isolated broken fibers within these composites using MRS. Guided by these in situ observations and measurements, we develop a single fiber model (SFM) to account for the influence of inelastic zones in a viscoelastic matrix. Notably this model provides the time dependent strain distributions and inelastic zone growth in closed form and agreement with MRS data not true of the viscoelastic model alone. Such a simplified model will find numerous applications in the area of composite lifetime prediction, but nonetheless, we conclude this paper with the relevant SFM model features that could be used in the development of a multifiber model.

Complementary objectives are (i) to determine the in situ parameters associated with the time dependent matrix and interface behavior and (ii) to quantify the influence of V_f on inelastic zone growth and on applicability of the SFM for multifiber composite specimen analysis. As we will demonstrate here, V_f can affect the type of inelastic zone that forms around the break. SFM models are often thought to be applicable only to low V_f composites in which fiber–fiber interactions are subtle, a concept which is intuitive but hard to substantiate.

2. Matrix creep compliance

In the present study, we assume the matrix is linearly viscoelastic in shear. In previous work (Zhou et al., 2002) the authors considered two models for matrix creep shear compliance $J(t)$. One was the following three-parameter power law, “complete law”

$$J(t) = J_c[1 + (\mathcal{T}/\mathcal{T}_c)^\alpha] = J_c[1 + t^\alpha] \quad \{\text{complete law}\} \quad (1)$$

where \mathcal{T} is real time, \mathcal{T}_c is the characteristic time constant for matrix relaxation, J_c is the initial elastic component of matrix compliance, and α is the viscoelastic exponent or shape parameter. In Eq. (1) above we define the normalized (dimensionless) time variable t ,

$$t = \mathcal{T}/\mathcal{T}_c \quad (2)$$

which we will use throughout the remainder of the paper, unless specified otherwise. Like (1), the other model, the “incomplete law”, was a three-parameter power law, but was found to represent well only the long time response of $J(t)$, $t > 1$,

$$J(t) = J_c(\mathcal{T}/\mathcal{T}_c)^\alpha = J_c t^\alpha \quad \{\text{incomplete law}\} \quad (3)$$

since it neglects the initial elastic response. As demonstrated in Lagoudas et al. (1989) and Zhou et al. (2002), composite models using (1) and (3) yield the same results for $t > 1$. The importance of considering (3) over (1) is that spatial and time dependence in the resulting composite model solutions can be coupled into one single variable (Beyerlein et al., 1998a,b; Beyerlein, 2000), making (3) extremely attractive for large-scale longtime, multifracture modeling and computational efficiency in simulation.

These functional representations of $J(t)$ greatly simplify the viscoelastic behavior of polymer materials. Though more representative viscoelastic material models (Aboudi, 1991; Schapery, 1964, 1967; Schapery et al., 1967) typically may have several distinct time constants, it is possible in some cases to fit creep data to much simpler expressions, like (1) or (3). In (1) and (3), a single time constant is used in power form with exponent α , which controls the rate of increase of the matrix compliance. For polymer materials, α lies in the range $0 \leq \alpha \leq 1$, wherein $\alpha = 0$ and 1 correspond respectively to linear elasticity and Newtonian viscosity. These power laws have been reduced to one-dimension from their three-dimensional fourth-order tensor form for use in our shear lag models. Also, the material parameters α , J_c or J_e , and \mathcal{T}_c could change with time, temperature and stress, but for simplicity, we assume they are constants at room temperature.

It should be emphasized that any analytical form for $J(t)$, in addition to (1) and (3), can be used in the SFM developed here, but because some of our measurement times are $t \ll 1$, we will use the complete law model (1) in the remainder of the paper.

3. Time dependent stress transfer model

In this section, we develop an analytical SFM, which combines the influences of matrix viscoelasticity and inelastic zone growth, primarily in the form of interfacial slipping and matrix shear yielding.

3.1. Assumptions and boundary conditions

Figs. 2 and 3 illustrate two different viewpoints of the axisymmetric SFM geometry, as it is represented within a multifiber composite. As viewed looking down the fiber axis, the SFM is intended to represent an axisymmetric unit cell in either a 2D or 3D fiber arrangement (Fig. 2a and b respectively). As shown in Fig. 3, a single fracture is located at $x = 0$ and a steady uniform load is applied far field.

The model applies classic shear lag assumptions. The matrix deforms or creeps only in shear, and prior to the onset of inelastic behavior, is linearly viscoelastic with creep shear compliance $J(t)$. The fibers have time-independent, elastic properties and sustain the axial stress (or strain) applied on the composite. Based on these assumptions, the model stresses and displacements will depend only on x , the fiber axial coordinate, and time t . The fiber displacement and strains and inelastic zone length $l(t)$ will be symmetric about x . (Thus in the remainder of the paper, we can operate in $0 \leq x \leq \infty$.)

The key problem is to find the fiber displacement $V(x, t)$ in x and in time t . The general equilibrium equation in $V(x, t)$ is

$$\frac{\partial^2 V(x, t)}{\partial x^2} - \frac{B}{AE} \tau_i(x, t) = 0, \quad 0 \leq |x| < \infty \quad (4)$$

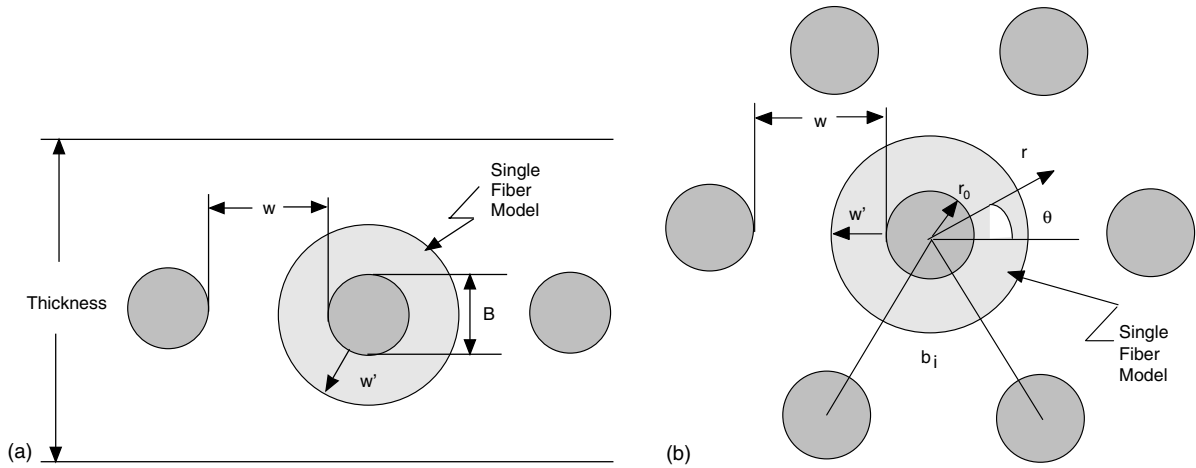


Fig. 2. Axisymmetric single fiber model bounded by the effective spacing w' within (a) a 2D planar fiber composite and (b) 3D model fiber composite with a low fiber volume fraction. The 2D arrangement best represents the multifiber composite specimens tested here.

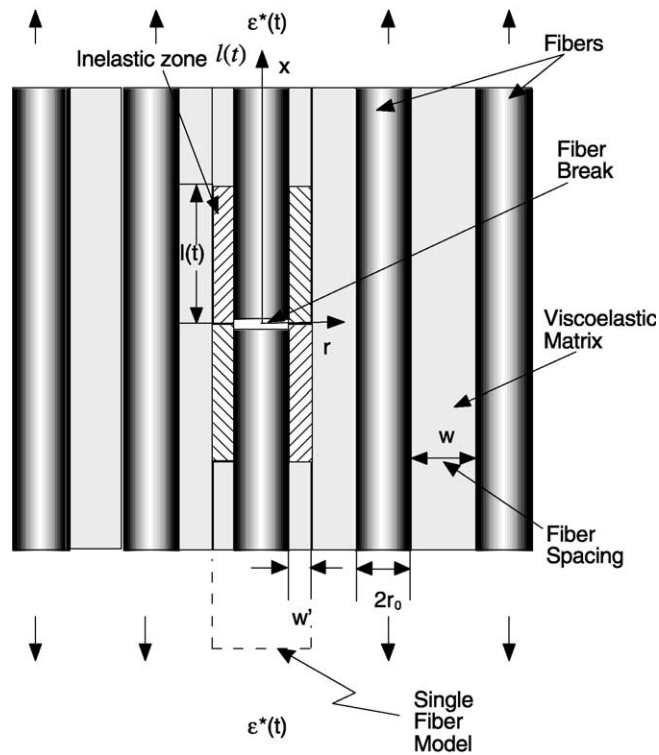


Fig. 3. Illustration of the inelastic zones emanating symmetrically from a single break in a model multifiber composite.

where $\tau_i(x, t)$ is the interfacial shear stress. In the above, we have made use of Hooke's law for the fiber, with Young's modulus E , and we assume the fiber is circular in cross-section, so $A = \pi r_0^2$ and $B = 2\pi r_0 = \pi d$, where r_0 and d are the fiber radius and diameter.

The boundary conditions¹ are

$$\partial V(x=0, t)/\partial x = \varepsilon_r(t) \quad (5a)$$

$$V(x = \pm\infty, t) = \varepsilon^*(t) \quad (5b)$$

which describe a time dependent residual strain $\varepsilon_r(t)$ measured within $\pm 1 \mu\text{m}$ of the fracture surfaces $x = 0$ and a fiber strain $\varepsilon^*(t)$ applied far field.² Under constant load, both $\varepsilon^*(t)$ and the far field strain in the matrix will show a variation in time as a result of the relaxation of the tensile stiffness of the matrix, though only the former $\varepsilon^*(t)$ is modeled here. In MRS studies involving polymer matrix composites a negative value of $\varepsilon_r(t)$ was persistently measured (Amer et al., 1995), being close to zero in thermosets and much larger in thermoplastics (Schadler et al., 1992). In our composites fabricated at room temperature, a nonzero measurement of $\varepsilon_r(t)$ is likely to result from matrix contraction due to curing.

For now, we make the assumption that the matrix shear stress and shear strain $\gamma(x, t)$ are independent of r , the radial distance from the center of the fiber as indicated in Fig. 2 or 3. Consequently $\gamma(x, t)$ is constant over the fiber spacing, w (see Figs. 2 and 3). At fixed time t and x , $\gamma(x, t)$ is related to the difference between $V(x, t)$ at $r = r_0$ (and also within the fiber, $0 < r < r_0$) and the axial displacement at $r = r_0 + w$, assumed to be $\sim \varepsilon^*(t)x$,

$$\gamma(x, t) = \frac{V(x, t) - \varepsilon^*(t)x}{r_0 + w - r_0} = \frac{U(x, t)}{w}, \quad 0 \leq |x| < \infty \quad (6)$$

where

$$U(x, t) = V(x, t) - \varepsilon^*(t)x, \quad 0 \leq |x| < \infty \quad (7)$$

3.2. Inelastic zone

For most of this work, the shear stress–displacement behavior of the matrix or interface close to the fiber is assumed to follow the elastic–inelastic constitutive law in Fig. 4. (Solutions for the more complex law in Fig. 12 can be found in the Appendix A.) The inelastic interfacial shear stress $\tau_d(t)$ is a function of time, but independent of space and can represent either matrix shear yielding or interfacial sliding friction of a failed interface. Previous MRS work (Zhou et al., 2002) indicates that there is a mild increase in $\tau_d(t)$ as the inelastic zone length $l(t)$ increases and time progresses. The creep of the matrix within $l(t)$ is ignored.

Over the slip length $0 \leq x \leq l(t)$ (Fig. 3), the equilibrium equation (4) simplifies to

$$\frac{\partial^2 V(x, t)}{\partial x^2} - \frac{B}{AE} \tau_d(t) = 0, \quad 0 \leq x \leq l(t) \quad (8)$$

Typically interface separation is thought to initiate when the interface reaches a critical shear stress or strength, τ_{crit} in Fig. 4. However, the peak interfacial shear stress τ_{max} decays in time and therefore cannot explain the time-growing inelastic zones observed experimentally. Rather as the matrix relaxes, the axial opening displacement of the fiber fracture surfaces and peak shear strain increase. Accordingly onset of an

¹ The same analysis can be also conducted by considering the problem of strain ($\varepsilon_r - \varepsilon^*$) applied to the fracture surface at $x = 0$ and zero strain applied in the far field $x = \pm\infty$.

² Values for the far field strain $\varepsilon^*(t)$ and $\varepsilon_r(t)$ used in the model are those measured in the fiber at each measurement time, though in principle any macroscopic composite model could be used for $\varepsilon^*(t)$ and $\varepsilon_r(t)$.

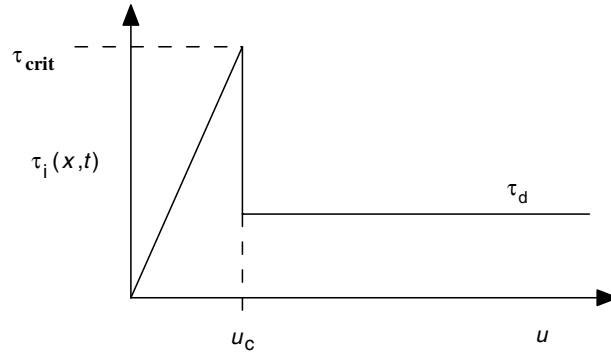


Fig. 4. Illustration of the elastic–inelastic law for the response of the interface or matrix material near the fiber surface.

inelastic zone is considered to occur when the bonded, elastic interface reaches either a critical value of the differential displacement $U(x, t)$, Eq. (7), denoted u_c in Fig. 4 or matrix shear strain γ_c at $x = 0$. We employ this criterion to define the slip length, $l(t)$, as follows³

$$u_c(x = l(t), t) = \gamma_c w \quad \text{where} \quad \gamma(x = l(t), t) = \gamma_c \quad (9)$$

We make the simplifying assumption that u_c and γ_c are time independent. Solving Eq. (8) with boundary conditions (5a) and (9) leads to the following for fiber displacement and strain in the inelastic zone

Inelastic Zone, $0 < x < l(t)$

$$V(x, t) = \frac{k_1 \tau_d(t)}{2} (x^2 - l(t)^2) + (\varepsilon_r(t) - \varepsilon^*(t))(x - l(t)) + u_c + \varepsilon^*(t)x \quad (10)$$

$$\frac{\partial V}{\partial x}(x, t) = k_1 \tau_d(t)x + \varepsilon_r(t) \quad (11)$$

$$k_1 = \frac{B}{AE}, \quad B = 2\pi r_0$$

3.3. Viscoelastic zone

The equilibrium equation (4) for the viscoelastic zone $l(t) \leq x < \infty$, is

$$\frac{\partial^2 V(x, t)}{\partial x^2} - \frac{B}{AE} \tau_i(x, t) = 0, \quad l(t) \leq x < \infty. \quad (12)$$

The interfacial shear stress in the matrix $\tau_i(x, t)$ is viscoelastic and changes in time according to

$$\tau_i(x, t) = \int_{-\infty}^t g(t - t') \frac{\partial \gamma}{\partial t'} dt' \quad (13)$$

³ Eq. (9) applies when neighboring fiber strains are neglected as in the single fiber model. When neighboring fiber interactions are considered, the expression for $\gamma(x, t)$ changes and consequently, $u_c \neq U(x = l(t), t)$.

where $g(t)$ is the shear modulus of the matrix. Substituting the constitutive relation (13) for $\tau_i(x, t)$ in Eq. (12) and using Eq. (6) for $\gamma(x, t)$, the equilibrium equation in $U(x, t)$ becomes

$$\frac{\partial^2 U(x, t)}{\partial x^2} - \frac{B}{wAE} \int_{-\infty}^t g(t-t') \frac{\partial U(x, t')}{\partial t'} dt' = 0, \quad l(t) \leq x < \infty \quad (14)$$

Note that we have made use of Eq. (7) and the fact that

$$\frac{\partial^2 V}{\partial x^2} = \frac{\partial^2 U}{\partial x^2}$$

In terms of $U(x, t)$, the boundary conditions become

$$U(x = l(t), t) = u_c \quad (15a)$$

$$\frac{\partial U(x = \pm\infty, t)}{\partial x} = 0 \quad (15b)$$

We assume that the fiber break does not occur until application of the load at $t = 0^+$. Thus all fibers are intact for $-\infty < t < 0^-$. Hence the initial conditions are

$$U(x, t = 0) = 0 \quad \text{and} \quad \frac{\partial U}{\partial t}(x, t = 0) = 0 \quad (16)$$

In Laplace transform space, the equilibrium equation (14) becomes

$$\frac{\partial^2 W(x, s)}{\partial x^2} - k_0^2 \bar{\mu}(s) W(x, s) = 0 \quad (17)$$

$$k_0^2 = \frac{B}{EA w J_0}$$

where we used

$$s \bar{G}(s) = \frac{\bar{\mu}(s)}{J_0} \quad (18)$$

In Eqs. (17) and (18), J_0 denotes the time independent compliance constant used in the creep compliance model of choice, either J_c of (1) or J_e of (3), s is the Laplace variable and $W(x, s)$ is the Laplace transform of the displacement difference $U(x, t)$. In general all other functions with an overbar, $\bar{f}(s)$, denote the Laplace transform of $f(t)$. The boundary conditions transform accordingly; at the inelastic zone front, $x = l(t)$, $W = u_c/s$ and in the far field, W must vanish.

We apply Schapery's approximate method for Laplace Transform inversion (Schapery et al., 1967) to transform $W(x, s)$ back to $U(x, t)$. According to the method, the inverse Laplace transform of $\bar{f}(s)$ is approximately,

$$f(t) \approx s \bar{f}(s) \big|_{s=\exp(-\gamma_s)/t}, \quad \alpha < 0.5 \quad (19)$$

where γ_s is Euler's constant, $\gamma_s \approx 0.5772$. We show in (Beyerlein et al., 1998a) that this approximation works very well when $\alpha < 0.5$ in model (1) or (3). Applying Eq. (19) and using the relation (7) between U and V , we obtain an approximation for the fiber displacement and strains, when $l(t) > 0$,

$$V(x, t) \approx u_c \exp[-K(t)(x - l(t))] + \varepsilon^*(t)x, \quad l(t) \leq x < \infty \quad (20)$$

$$\frac{\partial V(x, t)}{\partial x} \approx -u_c K(t) \exp[-K(t)(x - l(t))] + \varepsilon^*(t), \quad l(t) \leq x < \infty \quad (21)$$

where we define

$$K(t) = k_0 \sqrt{\mu(s)}|_{s=\exp(-\gamma_s)/t} = k_0 \sqrt{\mu(t)} \quad (22)$$

3.4. Time dependent inelastic length

Within the inelastic zone, $U(x, t) \geq u_c$ and outside $U(x, t) \leq u_c$; therefore $U(x, t) = u_c$ at $x = l(t)$. Equating Eqs. (11) and (21) at $x = l(t)$ to enforce continuity in fiber strain at $x = l(t)$ gives us

$$k_1 \tau_d(t) l(t) - (\varepsilon^*(t) - \varepsilon_r(t)) = -u_c K(t), \quad x = l(t)$$

or an expression for $l(t)$

$$l(t) = \max_{t>0} \left[\frac{((\varepsilon^*(t) - \varepsilon_r(t)) - u_c K(t))}{k_1 \tau_d(t)}, 0 \right] \quad (23)$$

We use $\max[\cdot]$ to define $l(t)$ by the maximum value of $l(t)$ over $t > 0$, not allowing $l(t)$ to heal itself, decrease in time, or be negative. Not surprisingly we find that $l(t)$ will be longer for higher $\varepsilon^*(t)$, lower τ_d or smaller w (since $u_c K(t)$ is proportional to $w^{1/2}$). Also with Eq. (23), one can determine the time at which an inelastic zone will initiate and the conditions under which $l(t)$ will grow under matrix creep. Expression (23) above for the time dependent slip length $l(t)$ completes the development of the model.

3.5. Summary

The final expressions for fiber displacement $V(x, t)$ and strain, $\varepsilon(x, t)$ around a single break at $x = 0$, are summarized below.

For $0 \leq |x| \leq l(t)$, the inelastic zone, when $l(t) > 0$

$$V(x, t) = \frac{k_1 \tau_d(t)}{2} (x^2 - l(t)^2) + \varepsilon_r(t)(x - l(t)) + u_c + \varepsilon^*(t)l(t) \quad (24)$$

$$\varepsilon(x, t) = \frac{\partial V}{\partial x}(x, t) = k_1 \tau_d(t)x + \varepsilon_r(t) \quad (25)$$

For $l(t) \leq |x| < \infty$, the viscoelastic zone, when $l(t) \leq 0$

$$V(x, t) \approx \frac{[(\varepsilon^*(t) - \varepsilon_r(t)) - k_1 \tau_d(t)l(t)]}{K(t)} \exp[-K(t)(x - l(t))] + \varepsilon^*(t)x \quad (26)$$

$$\varepsilon(x, t) = \frac{\partial V(x, t)}{\partial x} \approx [k_1 \tau_d(t)l(t) - (\varepsilon^*(t) - \varepsilon_r(t))] \exp[-K(t)(x - l(t))] + \varepsilon^*(t) \quad (27)$$

$$l(t) = \max_{t>0} \left[\frac{((\varepsilon^*(t) - \varepsilon_r(t)) - u_c K(t))}{k_1 \tau_d(t)}, 0 \right] \quad (28)$$

$$k_1 = \frac{B}{AE}, \quad B = 2\pi r_0$$

$$K(t) = k_0 \sqrt{\mu(t)} \quad (29a)$$

$$k_0^2 = \frac{B}{EA w J_0} \quad (29b)$$

The inelastic zone solutions above (24) and (25) are valid only when $l(t) > 0$. The purely viscoelastic case is recovered when $l(t) = 0$ in the viscoelastic solutions Eqs. (26)–(29). For convenience, we rewrite this case below:

For $l(t) = 0$ only

$$V(x, t) \approx \frac{[(\varepsilon^*(t) - \varepsilon_r(t))]}{K(t)} \exp[-K(t)x] + \varepsilon^*(t)x \quad (30)$$

$$\varepsilon(x, t) \approx [\varepsilon_r(t) - \varepsilon^*(t)] \exp[-K(t)x] + \varepsilon^*(t) \quad (31)$$

Using the same procedure, one can consider a more complex elastic–plastic-slipping law as depicted in Fig. 12, in the Appendix A, in which matrix shear yielding is followed by interfacial failure. Our SFM was extended for this more complex law. For brevity, only the fiber displacements⁴ and inelastic zone lengths that are associated with this extension are reported in the Appendix A.

To complete the calculation, one still needs to choose appropriate values for $\mu(t)$ in $K(t)$ Eq. (29) and w , which are discussed respectively in the next two following Sections 3.6 and 3.7.

3.6. Matrix creep compliance $J(t)$

The expression for $K(t)$ in the formulations depends on the model used for the matrix creep compliance. Finding $K(t)$ requires first an expression for $\mu(t)$ in Eq. (29), which is related to the matrix compliance or stiffness in Laplace space by

$$s\bar{G}(s) = \frac{1}{s\bar{J}(s)} = \frac{\bar{\mu}(s)}{J_0} \quad (32)$$

We choose to invert Eq. (32) using Eq. (19)⁵ to estimate $\mu(t)$. For example we summarize $\mu(t)$ for both creep compliance models in Section 2, Eqs. (1) and (3).

$$\mu_c(t) = \frac{1}{1 + k_2 t^\alpha} \quad \{\text{complete law, Eq. (1)}\} \quad (33)$$

$$\mu_c(t) = \frac{1}{k_2 t^\alpha} \quad \{\text{incomplete law, Eq. (3)}\} \quad (34)$$

$$t = \mathcal{T} / \mathcal{T}_c, \quad \{\text{normalized time}\}$$

$$k_2 = \Gamma(1 + \alpha) \exp(\alpha \gamma_s)$$

$$\gamma_s \approx 0.5772 \quad \{\text{Euler's constant}\}$$

3.7. Effective fiber spacing w'

In this section, we define an effective fiber spacing w' to be used in place of w in Eqs. (6), (9), and (29b). As illustrated in Fig. 2, the outer radius w' defines the boundary of the SFM intended to represent an

⁴ From the fiber displacements, all stresses and strains can be derived as in the elastic–inelastic case, Fig. 3, detailed in Sections 3.1–3.5.

⁵ Schapery et al.'s (1967) approximate Laplace transform inversion method Eq. (19) has been shown to work well for $\alpha < 0.5$ (Beyerlein et al., 1998a) which will be the case here (see Table 2).

axisymmetric unit cell in either a 2D or 3D fiber arrangement (Fig. 2a and b respectively). This empirical definition of w' will have some physical basis, and is meant only to adjust reasonably the boundary of the SFM when w is large, say $w > 4r_0$ where r_0 is the fiber radius. In this case, w could be too large to be used in (6) for calculating the matrix shear strains for two reasons, both related to the presence of matrix tension when w is large. First, the shear strains in the matrix will be inhomogeneous, being significant close to the fiber surface, but not elsewhere and thus (6) would underestimate the shear strains near the interface that are important for inelastic zone growth. For this shear decay we can consider the form

$$\tau_r(r, x) = \tau_i(x) \frac{r_0}{r} \quad (35)$$

where at the interface $r = r_0$, $\tau_r(x, r = r_0) = \tau_i(x)$. Second, matrix tension can limit the shear strains from decaying according to (6), that is, indefinitely as w increases. On the other hand, when w is small, on the order of r_0 matrix tension is negligible and (6) is a good description. These arguments lead us to define w' as

$$w' = r_0 \ln \left(\frac{r_0 + w}{r_0} \right), \quad w \geq r_0 \quad (36a)$$

$$w' = w, \quad w \leq r_0 \quad (36b)$$

where (36a) is derived from equating the average of (35) from $r = r_0$ to $r = w + r_0$ to τ_i over a distance w' . Note that $w' \approx w$, for $w = r_0$ in (36a).

After selecting $K(t)$ and w' in Sections 3.6 and 3.7, respectively, the remaining parameters needed for the SFM solution are material parameters, which are supplied by loading experiments and composite system data, as will be described in the results.

3.8. Interfacial shear stress

According to our SFM model, when using the elastic–inelastic law in Fig. 4, $\tau_i(x, t)$ will follow the profile in Fig. 1: it will be a constant $\tau_d(t)$ within $0 < x \leq l(t)$, achieve a maximum value $\tau_{\max}(t)$ at $x = l(t)$ and decay with x within the viscoelastic zone, $l(t) \leq x < \infty$ (see Fig. 1). From Eqs. (26) and (29), one can determine an expression for $\tau_i(x, t)$, within the viscoelastic zone, $l(t) \leq x < \infty$, which is

$$\tau_i(x, t) = \frac{EA}{B} K(t) [(\varepsilon^*(t) - \varepsilon_r(t)) - k_1 \tau_d(t) l(t)] \exp[-K(t)(x - l(t))], \quad l(t) \leq x < \infty \quad (37)$$

The maximum viscoelastic shear stress $\tau_{\max}(t)$ occurs at $x = l(t)$. We will consider two cases: times when $l(t) = 0$ and $l(t) > 0$. From (37) when $l(t) = 0$, $\tau_{\max}(t)$ at $x = 0$ decays in time as

$$\tau_{\max}(t) = \frac{EA}{B} K(t) (\varepsilon^*(t) - \varepsilon_r(t)), \quad \text{at } x = 0, \quad l(t) = 0 \quad (38)$$

until it reaches a critical value related to u_c which initiates an inelastic zone. For times when $l(t) > 0$, τ_{\max} then decays in time as

$$\tau_{\max}(t) = \frac{\mu(t)}{wJ_0} u_c \quad \text{at } x = l(t), \quad l(t) > 0 \quad (39)$$

where we have used the expression for $l(t)$, Eq. (23) or (28), in (37). When $l(t) > 0$, the absolute maximum interfacial shear stress $\tau_{\text{abs max}}$ will be the maximum of the elastic peak shear stress (39) and shear stress acting over the inelastic zone.

$$\tau_{\text{abs max}} = \max \left[\frac{\mu(t)}{wJ_0} u_c, \tau_d(t) \right], \quad l(t) > 0. \quad (40)$$

Note that when $l(t) > 0$, there is a discontinuity in the interfacial shear stress at $x = l(t)$. At $x = l(t)^-$, where the interface is inelastic, $\tau_i(x, t) = \tau_d(t)$. At $x = l(t)^+$, where the matrix is elastic and still bonded to the fiber, τ_{max} is governed by viscoelastic matrix relaxation and is limited by $\gamma_c = u_c w'$. Eq. (40) suggests that the $\tau_{\text{abs max}}$ is the larger of the two at any given time.

3.9. Length scales of load transfer

Using data surrounding a broken fiber like those in Fig. 1, one can measure $L_r(t)$, defined here as the distance between $l(t)$ and the point where $\tau_i(x, t)$ decays to a small fraction Ψ_i of $\tau_{\text{max}}(t)$. Applying this criterion $\tau_i(x = L_r(t) + l(t), t) / \tau_{\text{max}}(t) \approx \Psi_i$ where typically, $0.02 < \Psi_i < 0.1$, we get for $L_r(t)$

$$L_r(t) = -\frac{\ln \Psi_i}{K(t)} \quad \text{or} \quad L_r(t)k_0 = A_r(t) = -\frac{\ln \Psi_i}{\sqrt{\mu(t)}} \quad (41)$$

where $A_r(t)$ is the normalized load recovery length.⁶ Notably $L_r(t)$ as defined by (41) is independent of both applied strain and $l(t)$ and increases roughly as $t^{\alpha/2}$. Furthermore, $A_r(t)$ is governed entirely by matrix relaxation and therefore its evolution will be the same for all samples tested here.

4. Experimental procedure

4.1. Preparation of model composite specimen

Fig. 5 shows the geometry of the multifiber composites fabricated for the creep tests. Each composite consisted of a planar array of relatively uniformly spaced 5–8 fibers bordered by graphite fiber tows to reduce macroscopic creep during the constant stress tests. The matrix material is an epoxy (Epon828 + Epi-Cure3234 curing agent at 1:0.129 ratio) and the graphite fiber is a high modulus Toray M4OB. The materials properties are shown in Table 1. The gauge section was 40 mm (length) \times 5 mm (width) and the final thickness of the samples was ~ 2 mm ($\sim 600 r_0$). We refer the reader to (Zhou et al., 2002) for more details on composite fabrication.

4.2. Composite creep tests

Composite creep tests were performed at room temperature, $\sim 25^\circ\text{C}$. A constant uniform stress was applied to the samples using custom-built jigs and a strain gage was attached to the surface to monitor the

⁶ One commonly finds that $L_r(t)$ is, instead, defined by a cutoff fiber strain, $\varepsilon(L_r(t) + l(t), t) / \varepsilon^* \approx \Psi_F$ where typically, $0.02 < 1 - \Psi_F < 0.1$. These two definitions provide nearly equivalent estimates for $L_r(t)$ when the inelastic length, $l(t)$, is short. However it can be shown that these two definitions do not lead to the same value for $L_r(t)$ when the length of the inelastic zone is long, or when

$$l(t) > \frac{E\varepsilon^* r_0}{8\tau_d} \quad (42)$$

This more commonly used definition of $L_r(t)$ predicts that $L_r(t)$ increases roughly as $t^{\alpha/2}$ when $l(t) = 0$ and as $t^{\alpha/2} \ln(t^{\alpha/2})$ when $l(t)$ grows to an extent where Eq. (42) is satisfied.

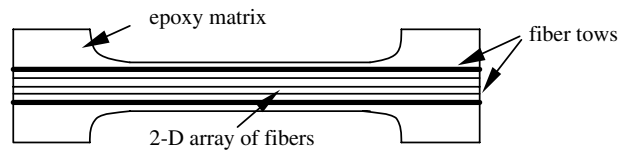


Fig. 5. Geometry of the composite specimens tested in this work.

Table 1

Material properties of the graphite fiber and the epoxy matrix used in the composite specimens

Material properties	Fiber	Epoxy matrix
Young's modulus (GPa)	390	3.35
Shear modulus (GPa)	147	1.26
Poisson ratio	–	0.33
Fiber diameter (μm)	6.6	–
Fiber cross-section area (μm^2)	34.2	–

macro-strain. The applied load was increased until a break was observed in a fiber and then held constant. Macro-creep was negligible during the testing period, starting at 5 min and ending after as much as 29 days.

A Renishaw Ramanscope System 2000 connected to a 514 nm Argon ion laser was used to record the Raman spectra of the fiber during the creep tests. Toray M40 fibers have a very well defined Raman peak around 2700 cm^{-1} , corresponding to the second order A_{1g} mode, which shifts linearly to lower values as the fiber tensile strain increases. The slope of this linear relationship, the Raman frequency gauge factor (RFGF), is $25.35 \pm 2\text{ cm}^{-1}/\%$ for the Toray M40 fiber. The axial strain $\varepsilon(x, t)$ at any point x along a high performance fiber at time t can be determined according to

$$\varepsilon(x, t) = (v(x, t) - v_0)/\text{RFGF}, \quad \text{at a given measurement time} \quad (43)$$

where $v(x, t)$ and v_0 are the peak positions at point x and time t and at zero strain respectively. From the Raman spectra of the Toray M40 fiber, we can determine the in situ fiber strain with a spatial resolution of $\approx \pm 1\text{ }\mu\text{m}$. Subsequently, once the fiber strain is known, all other stress/strain fields can be determined from the model.

Raman spectra were recorded along the fibers at periodic time intervals, starting at 5 min and ending after several weeks. The time required to record a single measurement was 20 s. Approximately 60 data points were collected along a single fiber. Therefore the time required for one fiber profile was $\approx 20\text{--}30\text{ min}$ and the time of measurement is associated with the time at the start of each acquisition period. The error in the strain measurement is $\approx \pm 0.05\%$.

5. Results

5.1. Creep of the bulk epoxy matrix

In previous work (Zhou et al., 2002), we performed a series of constant load, room temperature creep tests (up to 20 days) to estimate the values of the parameters for both (1) and (3). Table 2 summarizes the estimates from fitting the complete power law Eq. (1) with the data. It was found that the complete power law was capable of representing the data over the entire testing period at fixed applied load.

Table 2

Parameters associated with the matrix creep compliance function, “complete law”, Eq. (1), estimated from unreinforced epoxy matrix creep data (Zhou et al., 2002)

Parameters	Compliance constant J_1 (1/GPa)			Characteristic time constant \mathcal{T}_c (s)			Shape parameter α		
	10	20	30	10	20	30	10	20	30
Complete power law $J(\mathcal{T}) = J_1 + J_1(\mathcal{T}/\mathcal{T}_c)^\alpha$	0.78	0.78	0.88	1.4×10^9	1.9×10^8	7×10^7	0.26	0.21	0.23

We performed these bulk matrix creep tests over a load range similar to that used on the composite. Estimates listed in Table 2 indicate that α does not vary significantly over stress levels from 10 to 30 MPa when using the same compliance law. Thus the polymer matrix creeps at nearly the same rate for this range of stress levels at room temperature for both short and long times. In the following we will use estimates for the compliance parameters from creep data at an applied stress level of 20 MPa.

5.2. Comparison of MRS measurement and model predictions

Table 3 lists the measurement times, strain levels and w of the specimens analyzed. For each measurement time, the measured far field fiber strain, matrix strain, and residual strain at the fracture site are given. We find that both $\varepsilon^*(t)$ and $\varepsilon_r(t)$ did vary, $\varepsilon^*(t)$ more so than $\varepsilon_r(t)$. The initial far field residual strain in the matrix due to curing and cooling was ~ 0.3 – 0.4% , whereas $\varepsilon_r(t)$ at the break site was typically zero or slightly less than zero during the entire testing period. Considering the error in the measurement, within $\pm 0.05\%$, $\varepsilon_r(t)$ was also quite steady over the testing period, up to 29 days. As listed in Table 3, our samples varied in applied stress level and w , from extremely small, $\sim r_0/3$, up to $\sim 13r_0$.

5.2.1. Composites with no inelastic zones: time dependent fiber strain

Fig. 6 compares the model predictions and MRS results for fiber strain in sample 1, wherein no inelastic zones were observed, i.e. $l(t) = 0$, over the test period. Without adjusting any parameters, the agreement between the model and the data is very good. Calculations for sample 2, which also did not have inelastic zones, show similar behavior and agreement. Compared to the other specimens, V_f and strain levels in these two specimens were low. Under these conditions and assuming $\gamma_c = 4.5\%$ and $\tau_d = 20$ MPa, the model predicts that slipping will initiate at $\mathcal{T} = 1e + 9$ s, which is at the end of the testing period for samples 1 and 2.

5.2.2. Composites with inelastic zones: Interface characterization

Interface parameter characterization is a challenging problem particularly when multiple mechanisms (matrix relaxation, interfacial slipping, matrix shear yielding) are involved. For this reason, the simpler elastic–inelastic interface law (Fig. 4) with fewer parameters to characterize, only γ_c (or u_c) and τ_d was considered. These two parameters embody the essential physics of interface failure; $\gamma_c(u_c)$ is the critical strain (displacement) initiating slipping or “yielding” and τ_d is the slip shear stress after initiation.

Analyzing inelastic zones from a single break also facilitates characterization of these parameters considerably (He et al., 1999; Beyerlein et al., 1998b). Of the six samples tested, inelastic zones were evident from MRS fiber strain measurements of isolated fractures in samples 3–6, having either a relatively high applied strain or close fiber–fiber spacing, w , or both. In these samples, inelastic behavior presented itself as a linear region in the fiber profile with a slope proportional to τ_d as illustrated in Fig. 1. These inelastic zones likely initiated immediately after fiber fracture and grew in time. Not motivated otherwise by experimental observation, we assume u_c or $\gamma_c = u_c/w'$ is independent of space and time and τ_d is independent of space in their characterization.

Table 3

Experimental testing details: testing times, fiber spacing, and strain levels for the six laminar model composite specimens analyzed in this work

Sample no.	Fiber spacing w (μm)	Far field fiber strain/residual strain (%)		Measurement time (s)	Matrix strain (%)	Inelastic zones
S1	36	0.23	−0.1	1.8×10^3	0.5	Undetected
		0.24	−0.1	9.0×10^3	0.5	
		0.25	0	5.5×10^4	0.51	
		0.33	−0.03	4.0×10^5	0.6	
		0.37	−0.1	9.3×10^5	0.58	
S2	35	0.28	−0.06	6.0×10^2	0.61	Undetected
		0.28	−0.08	1.8×10^3	0.67	
		0.29	−0.04	3.3×10^3	0.69	
		0.29	−0.01	2.0×10^4	0.71	
		0.29	−0.03	9.4×10^4	0.70	
		0.37	−0.05	2.5×10^5	0.80	
		0.39	−0.03	7.7×10^5	0.85	
S3	40	0.55	−0.08	3.0×10^2	0.76	Detected
		0.56	−0.05	2.1×10^3	0.77	
		0.58	−0.09	6.6×10^3	0.78	
		0.61	−0.1	1.0×10^5	0.79	
		0.67	−0.07	8.8×10^5	0.85	
S4	44	0.64	−0.1	1.8×10^4	0.96	Detected
		0.64	−0.1	2.3×10^5	0.97	
		0.64	−0.1	5.7×10^5	0.98	
		0.65	−0.12	8.3×10^5	0.98	
		0.65	−0.13	1.6×10^6	1.01	
S5	~1 (four fibers)	0.74	−0.05	1.8×10^3	1.68	Detected
		0.76	−0.06	7.2×10^3	1.72	
		0.77	−0.1	2.9×10^4	1.74	
		0.78	−0.12	9.0×10^4	1.77	
S6	13	0.83	0.04	1.8×10^4	1.0	Detected
		0.82	−0.03	1.0×10^5	1.0	
		0.84	0.03	2.8×10^5	1.0	
		0.82	−0.04	8.0×10^5	1.05	
		0.84	−0.01	1.5×10^6	1.1	
		0.84	−0.03	2.5×10^6	1.15	

Values for a constant frictional $\tau_d(t)$ and $l(t)$ are estimated from fitting Eq. (25) to the linear portion of the MRS fiber strain data at each measurement time for samples 3–6. In some instances, we obtain two measurements for $l(t)$ at one time, one on each side of the break site. Table 4 lists the estimated τ_d and measured $l(t)$ for each sample over the testing period. The error in this measured value of $l(t)$ is $\pm 10 \mu\text{m}$.

As shown in Fig. 7, τ_d ranged from 20 to 40 MPa, over the time period, depending on sample and slightly on time. Note that 40 MPa is close to the maximum shear strength of the unreinforced matrix. Results in Fig. 7 suggest two relevant shear stresses, shear yielding at ~ 40 MPa for S5 and S6 and interfacial slipping at ~ 20 – 30 MPa for S3 and S4. For the slipping cases, τ_d appears to increase in the last measurement time from 20 to 30 MPa. However, rather than use the τ_d estimate at each time or fit the data in Fig. 7 to some mathematical form for $\tau_d(t)$, we elected to use, for practical reasons, a constant value for $\tau_d(t)$ of 20 or 30 MPa for interfacial slipping and 40 MPa for matrix shear yielding in the SFM calculations.

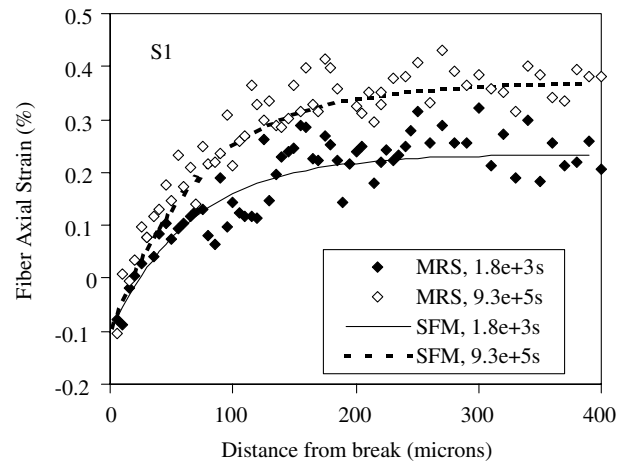


Fig. 6. Comparison of the MRS measured and SFM predicted fiber strain profiles for two different measurement times for sample 1. Sample 2 yields similar results and agreement. See Tables 1 and 4 for sample details.

Table 4
Interfacial characteristics and parameters estimated for each specimen

Sample no.	w' (μm)	γ_c (%)	τ_d (MPa)	Measured $l(t)$ (μm)	Predicted $l(t)$ (μm)	Near the break
S1	8.2	>3.7	N/A	0	0	Elastic
S2	8.1	>3.7	N/A	0	0	Elastic
S3	8.5	4.8	20	10–30	7–28	Slipping
S4	8.8	4.8	30	25–50	28–40	Slipping
S5	~ 1.0	4.6	40	~ 100	95–105	Plastic
S6	5.3	4.2	40	~ 70	65–75	Plastic

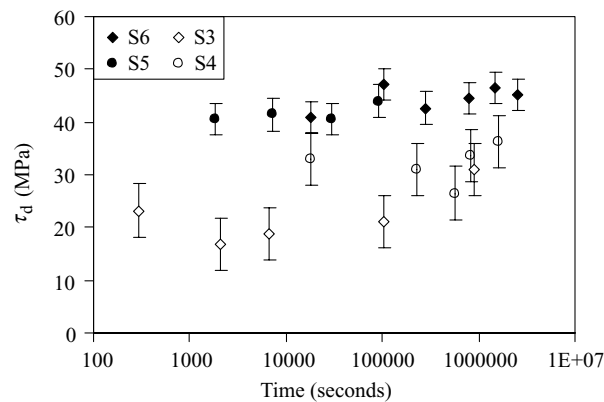


Fig. 7. Estimates for the constant interfacial shear stresses in the inelastic zone versus time.

Values for γ_c or u_c are estimated from fitting model strains, Eqs. (25) and (27), to measured MRS strains and using the corresponding values for $l(t)$ and τ_d in Table 4. Fig. 8 displays the dependence in u_c and γ_c for each sample w . Error in the measurement of $l(t)$ contributed to the variation in estimates of u_c . The average

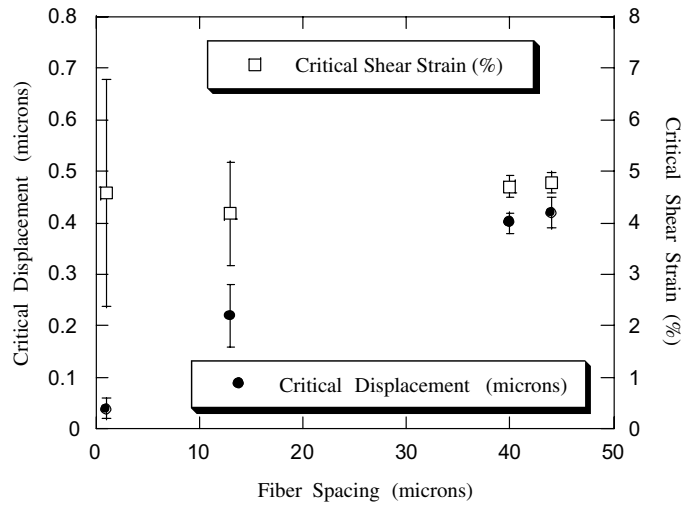


Fig. 8. Critical shear strain γ_c and critical displacement u_c for initiation of inelastic zones as a function of fiber spacing.

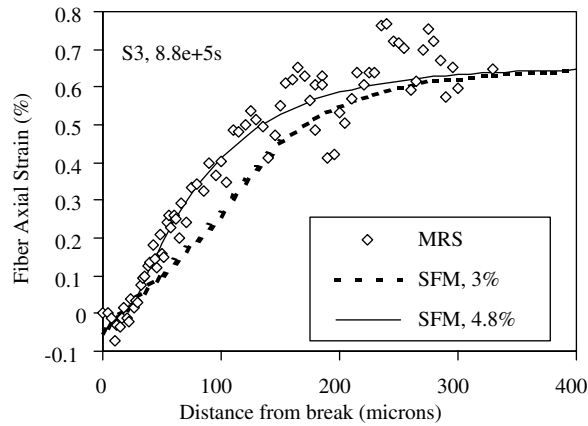


Fig. 9. Comparison of the MRS measured and SFM predicted fiber strain profiles for two different values of γ_c at one measurement time for sample 3.

value and variation in γ_c are calculated directly from u_c by $\gamma_c = u_c/w$ and consequently the range of possible values for γ_c increases for smaller w . Unlike u_c the average γ_c is relatively independent of w and thus is likely a material property of the interface. Table 4 shows the average values for γ_c used in the model, ranging from 4.2% to 4.8%, as well as the predicted variation in $l(t)$, Eq. (28), over the test period. As an example, Fig. 9 shows that $\gamma_c = 4.8\%$ gives a nice fit compared to $\gamma_c = 3\%$, at one measurement time for sample 3 ($\tau_d = 20$ MPa).

Estimates for τ_d were obtained assuming that τ_d is spatially constant over the entire inelastic length. These inelastic zones may, however, contain a mix of matrix shear yielding at high τ_p and interfacial slipping at low τ_d following the interface response in Fig. 12. However our calculations show that for these samples, using the elastic–plastic–slipping model (see Appendix A) did not result in significantly different

estimates for the interface parameters, suggesting that the inelastic zones were predominately slipping or yielding.

5.2.3. Composites with inelastic zones: time dependent fiber strain profiles

Fig. 10 compares the model predictions and MRS results for fiber strain in those specimens in which inelastic zones were detected, samples 3–6, due to high strain levels and/or high fiber volume fractions V_f . For this comparison we display one relatively short and long measurement time. The fiber strain predictions used the predicted value for $l(t)$ Eq. (28), corresponding measured values for $\varepsilon^*(t)$ and $\varepsilon_r(t)$ (see Table 3) and constants, τ_d and γ_c as listed in Table 4.

Fig. 10a and b shows the fiber strain profiles for the lowest V_f specimens we tested, samples 3 and 4, which had slip zones emanating from the break (see Table 4). Fig. 10c and d present the same comparison for the highest V_f samples, 5 ($w = 1 \mu\text{m}$) and 6 ($w = 13 \mu\text{m}$), wherein matrix shear yielding emanated from the break site (see Table 4), rather than interfacial slipping. Notably the SFM with the elastic–inelastic zone law Fig. 3 using average values for τ_d and γ_c generally describes the MRS measured time dependent profiles very well without any need for adjustment. Incidentally we obtain similar agreement for other measurement times or when the measured values for $l(t)$ were used rather than Eq. (28).

5.3. The maximum shear stress and load recovery length

MRS measurements and model predictions demonstrate that the fiber strains in these specimens did not change significantly when inelastic zones are present (Fig. 10), despite the large difference in measurement times. However, what is not obvious from these plots is the time evolution of the maximum shear stress τ_{\max}

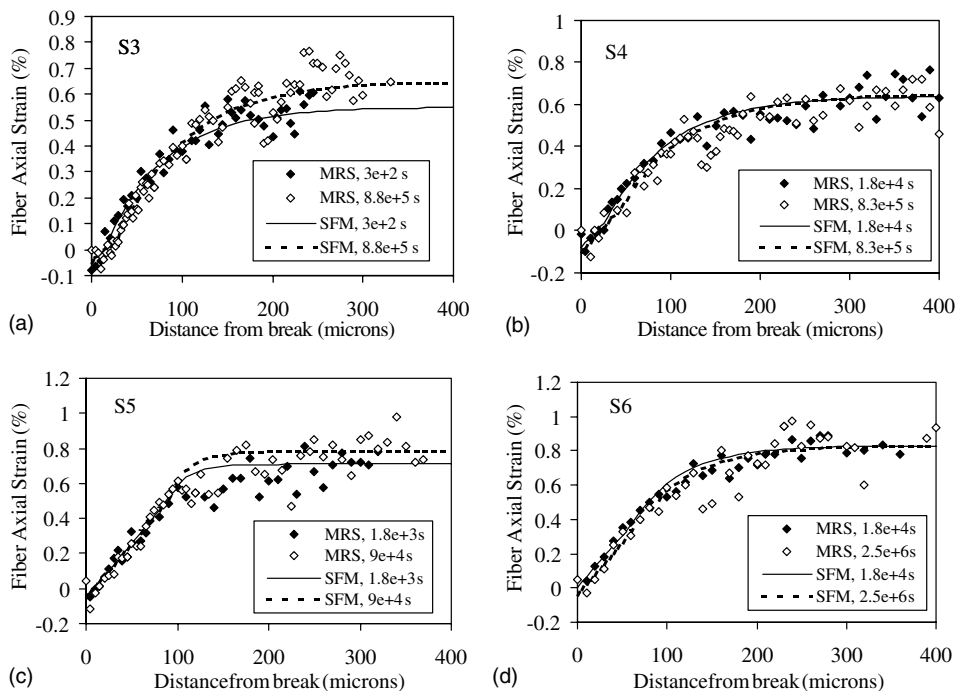


Fig. 10. Comparison of the MRS measured and SFM predicted fiber strain profiles for two different measurement times for (a) sample 3, (b) sample 4, (c) sample 5, and (d) sample 6. See Tables 1 and 4 for sample details.

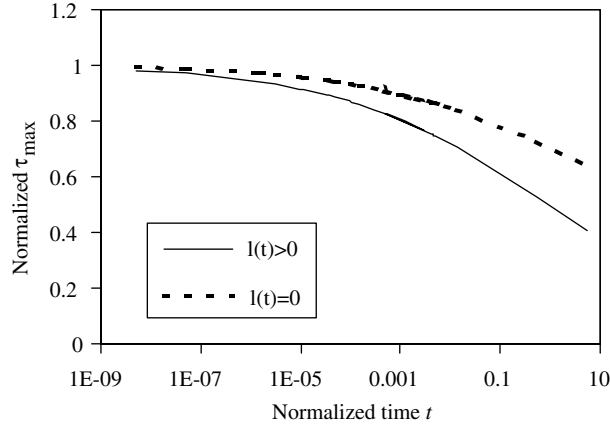


Fig. 11. Relaxation of the peak shear stress in time for samples 1 and 2 without inelastic zones and samples 3–6 with inelastic zones. The normalization of the peak shear stress for these two cases are different; please see text for definitions.

and load recovery lengths $L_r(t)$, which over large time differences can be significant. These parameters were observed to decay in time in both cases, with and without a slipping zone front. Using matrix (Tables 1 and 2) and in situ interface properties determined in Section 5.2.2, the SFM, Eqs. (38)–(41), can determine the time evolution of τ_{\max} and $L_r(t)$ and the important transitions in their behavior due to inelastic zones.

We first introduce normalizations so that evolution of τ_{\max} for different samples can be expressed on one curve. Expression (38) for $\tau_{\max}(t)$ when $l(t) = 0$ suggests that we can define a normalizing shear stress τ^* , as

$$\tau^*(t) = \frac{EAk_0(\varepsilon^*(t) - \varepsilon_r(t))}{B} = \sqrt{\frac{EA}{J_0 w' B}}(\varepsilon^*(t) - \varepsilon_r(t)) \quad (44)$$

Expression (39) for τ_{\max} in the case of $l(t) > 0$ leads to a simple normalization for shear stress,

$$\tau_0 = \gamma_c / J_0 \quad (45)$$

which is independent of time, applied strain and fiber properties.

In Fig. 11, we plot the normalized maximum shear stress τ_{\max}/τ^* for samples 1 and 2, wherein no inelastic zones were detected, and the normalized shear stress τ_{\max}/τ_0 for samples 3–6, wherein inelastic zones were detected. As shown, τ_{\max} decays at a noticeably faster rate in samples with time-growing inelastic zones than those without. Without an inelastic zone, the model predicts that τ_{\max} decays roughly as $t^{-\alpha/2}$ (or more precisely as $(1 + t^\alpha)^{-1/2}$) in Eq. (38), whereas in the presence of an inelastic zone, τ_{\max} decays as $t^{-\alpha}$ (39). The model also predicts that τ_{\max} is dependent on the strain level when $l(t) = 0$ but not when $l(t) > 0$.

6. Discussion and conclusions

Comparison between our model and this set of MRS data enabled us to fully characterize the in situ matrix and interfacial parameters of the composite, while using unreinforced matrix creep data fit to a simple viscoelastic matrix creep law. This comparison also helped to validate several new criteria employed in our model.

- (1) We introduce a new criterion for slip initiation and propagation in the presence of a viscoelastic matrix. This criterion is shear strain-based because the matrix shear strain close to the fiber surface increases in

time thereby initiating and propagating inelastic zones. This critical shear strain proves to be relatively independent of w , unlike the displacement criterion, and thus is a material parameter.

- (2) We also introduce an effective spacing, which defines the distance from the fiber surface at which local shear deformation is significant and enables application of the single fiber model to our multifiber composite samples over a wide range of fiber volume fractions. The failure mechanisms near breaks depend on the local w and thus characterization of the interface properties is more accurate via tests performed on multifiber composite specimens rather than single fiber composite specimens. Therefore it is important that this effective spacing w' or the outer radius (see Fig. 2) of the SFM is selected carefully, rather than used as an adjustable model parameter.
- (3) A criterion must also be employed to define the load recovery length from a fracture site, a useful characteristic length measuring stress transfer. We demonstrate here that a criterion based on a cutoff shear stress is independent of the inelastic zone and applied strain.

We find that the type of inelastic zone, shear yielding or interfacial slipping (or both), depends on the w' . When w' is large, the matrix is largely elastic and interfacial slipping is favored, but when w' is small, approximately a few microns, plastic-like matrix behavior is observed to emanate from the fracture site prior to interfacial slipping. Furthermore, we find that the critical displacement at which plastic behavior initiates is lower than that for interfacial slipping with a much larger w' .

These observations are likely consequences of either a size effect in material behavior or strain gradient effects in the matrix or both. If one can consider materials with $\sim 40\text{ }\mu\text{m}$ dimensions as possessing bulk properties, then we may be observing a transition to more plastic-like behavior in the epoxy due to size effects as the w decreases from $\sim 40\text{ }\mu\text{m}$, in samples 3 and 4, to $\sim 1\text{ }\mu\text{m}$ in samples 5. Similar geometrical size effects have been observed in bulk polymers versus thin polymer films a few microns thick (Gulino et al., 1991; Glad, 1986). It was shown in these works that unlike their otherwise brittle bulk counterparts, thin film epoxy withstands a significantly larger strain prior to failure. Otherwise it is possible that low radial strain gradients, existing when w is small, promote yielding whereas large radial gradients, existing when w is large, allow elastic shear strains in the matrix and interfacial slip to dominate.

The single fiber model and MRS data agree extremely well for a wide range of fiber volume fraction specimens despite the many modeling simplifications made: one dimensional stress state, time independent interface properties, a three-parameter matrix creep law, and no fiber neighbor interactions. This further demonstrates the significance of accounting for inelastic zones, for such agreement would not have been achieved otherwise (Zhou et al., 2002). Nonetheless, we discuss some of the model simplifications in light of the present results.

We assume in the calculations that the shear stress acting over the inelastic zones is constant in space and time. If experimental evidence suggest otherwise, the SFM developed here can treat these cases. For instance we extend the model to consider a more complex elastic–plastic-slipping law Fig. 12, allowing for a ‘mix’ of yielding and slipping in the inelastic zones. However for these samples, the simpler elastic–inelastic law in Fig. 4 was adequate. When the inelastic region was primarily shear yielding, τ_d was $\sim 40\text{ MPa}$ and did not vary in time during the test period. The frictional τ_d on the other hand, was found to be lower, varying from 20 to 30 MPa over time and between the two samples, S3 and S4. In addition, this frictional $\tau_d(t)$ was found to increase slightly at the longest measurement time, likely due to some source of increased lateral pressure on the interface (e.g. axial relaxation of the matrix or axial contraction of the fiber). Incidentally we have observed that inelastic zones stop growing after a long period of time, which would occur if τ_d were to increase, with all else being equal, according to Eq. (23). Though the SFM solutions allow for time dependence of τ_d , we elected to assume a fixed τ_d in the calculations until there is more understanding of the nature of its time evolution.

In this work we consider a simple creep compliance model, which has only three parameters, one of which is the characteristic time constant, observed experimentally to be sensitive to applied load. These

parameters are also likely to change with time as the polymer ages (Brinson and Gates, 1995). Despite the fact that our calculations assume that these three parameters are independent of stress and time, the model predictions performed well when using the unreinforced matrix creep properties fit to this model.

Though the SFM performed well for the wide range of V_f specimens tested it will have limitations in predicting failure processes. We intend to treat fiber–fiber interactions and stress concentrations by extending the present single fiber model to a multifiber one. The features which we suggest be included at the multifiber level are the time dependent inelastic zone length, a critical shear strain criterion for initiation and growth of the inelastic zone, the spatially constant inelastic zone shear stress $\tau_d(t)$ and a simple three-parameter matrix creep compliance model fit to unreinforced matrix properties.

Acknowledgements

This work was supported by National Science Foundation (No. CMS-9800128) and a Directed Research and Development Project at Los Alamos National Laboratory (No. 2000043). The authors also appreciated the technical assistance from Mr. D. Van Steele and Mr. R. Dove at Rensselaer Polytechnic Institute. This work was performed under the auspices of the United States Department of Energy.

Appendix A. Solution for elastic–plastic-slipping law, Fig. 12

Fig. 12 is a schematic of the elastic–plastic-slipping matrix response which has been proposed for the interface or matrix material near the interface (Gulino et al., 1991; Beyerlein et al., 1998b; Beyerlein and Phoenix, 1997). Here we extend our SFM for this more complex law. Unlike the elastic–inelastic response, there are many more parameters involved as indicated in Fig. 12: u_p the critical displacement for inelastic matrix behavior at shear stress τ_p , and u_{deb} , the critical displacement for slipping at shear stress τ_d . For brevity, only the fiber displacements⁷ and inelastic zone lengths are reported. In the following, it is assumed that $\tau_p \geq \tau_d$, and the extent of the plastic and slipping zone lengths, l_p and l_d , are measured from $x = 0$, so that $l_p \geq l_d \geq 0$.

For $0 \leq x \leq l_d(t)$, the fiber displacement within the slip zone $V_d(x, t)$ is

$$V_d(x, t) = \frac{k_1 \tau_d}{2} (x^2 - l_d(t)^2) + \varepsilon_r(t)(x - l_d(t)) + \varepsilon^*(t)l_d(t) + u_{deb} \quad (\text{A.1})$$

For $l_d(t) \leq x \leq l_p(t)$, the fiber displacement within the plastic region $V_p(x, t)$ is

$$V_p(x, t) = \frac{k_1 \tau_p}{2} (x^2 - l_p(t)^2) + [\varepsilon_r(t) - k_1 l_d(t)(\tau_p - \tau_d)](x - l_p(t)) + \varepsilon^*(t)l_p(t) + u_p \quad (\text{A.2})$$

For $l_p(t) \leq x < \infty$, the fiber displacement in the viscoelastic zone $V_e(x, t)$ is

$$V_e(x, t) = u_p \exp[-K(t)(x - l_p(t))] - \varepsilon^*(t)x \quad (\text{A.3})$$

where the extent of the plastic region measured from the break site $x = 0$ is

$$l_p(t) = \max_{t > 0} \left[\frac{(\varepsilon^*(t) - \varepsilon_r(t)) - u_p K(t)}{k_1 \tau_p} + \frac{(\tau_p - \tau_d)}{\tau_p} l_d(t), 0 \right] \quad (\text{A.4})$$

⁷ From the fiber displacements, all stresses and strains can be derived as in the elastic–inelastic case, Fig. 4, detailed in Sections 3.1–3.5.

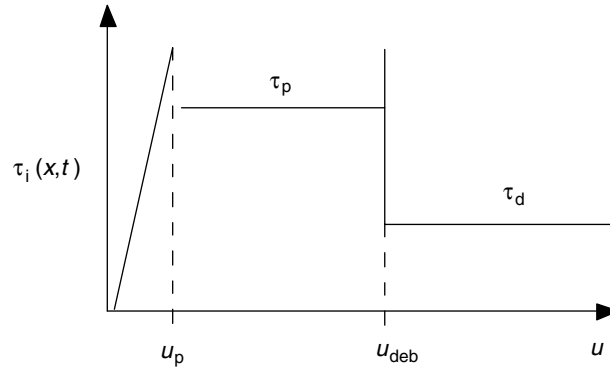


Fig. 12. Illustration of the elastic–plastic-slipping law for the response of the interface or matrix material near the fiber surface.

and the extent of the slip region from the break site $x = 0$ is

$$l_d(t) = \max_{t > 0} \left[\frac{(\varepsilon^*(t) - \varepsilon_r(t)) - \sqrt{(u_p K(t))^2 + 2k_1 \tau_p (u_c - u_p)}}{k_1 \tau_d}, 0 \right]. \quad (\text{A.5})$$

In the above, the plastic zone length is $l_p(t) - l_d(t)$. Note that if we set $\tau_p = \tau_d$ and $u_p = u_{deb} = u_c$, then we recover the elastic–inelastic constitutive law in Fig. 4 and $l_d(t) = l_p(t) = l(t)$ in Eq. (28).

References

- Aboudi, J., 1991. *Micromechanics of composites: a unified micromechanical approach*. Elsevier, New York.
- Amer, M.S., Koczak, M.J., Schadler, L.S., 1995. Environmental degradation of the interface in graphite/epoxy single filament composites using laser Raman spectroscopy: The effect of boiling water. *Compos. Interf.* 3, 41–50.
- Beaumont, P.W.R., Phillips, D.C., 1967. Tensile strengths of notched composites. *J. Compos. Mater.* 6, 32–46.
- Beyerlein, I.J., Phoenix, S.L., 1997. Stress profiles and energy release rates around fiber breaks in a lamina with propagating zones of matrix yielding and debonding. *Compos. Sci. Technol.* 57, 869–885.
- Beyerlein, I.J., Phoenix, S.L., Raj, R., 1998a. Time evolution of stress redistribution around multiple fiber breaks in a composite with viscous and viscoelastic matrices. *Int. J. Solids Struct.* 35 (4), 3177–3211.
- Beyerlein, I.J., Amer, M.S., Schadler, L.S., Phoenix, S.L., 1998b. New methodology for determining in situ fiber, matrix, and interface stresses in damaged multifiber composites. *Sci. Eng. Compos. Mater.* 7, 151–204.
- Beyerlein, I.J., 2000. Stress fields around cracks with a viscous matrix and discontinuous fiber bridging. *Compos. Sci. Technol.* 60, 2309–2326.
- Brinson, H.F., Griffith, W.I., Morris, D.H., 1981. Creep rupture of polymer-matrix composites, In: *Proc. IV Int. Cong. on Exp. Stress Anal. and Exp. Mech.*, pp. 329–335.
- Brinson, H.F., Dillard, D.A., 1982. The prediction of long term viscoelastic properties of fiber reinforced plastics. In: *Progress in Science and Engineering of Composites*, pp. 795–802.
- Brinson, L.C., Gates, T.S., 1995. Effects of physical aging on long term creep of polymers and polymer matrix composites. *Int. J. Solids Struct.* 32 (6,7), 827–846.
- Glad, M.D., 1986. *Microdeformation and network structure in epoxies*. Ph.D. Thesis., Cornell University, New York.
- Gulino, R., Schwartz, P., Phoenix, S.L., 1991. Experiments on shear deformation, debonding and local load transfer in a model graphite/glass/epoxy microcomposite. *J. Mater. Sci.* 26, 6655–6672.
- He, J., Beyerlein, I.J., Clarke, D.R., 1999. Load transfer from broken fibers in continuous fiber Al203–Al composites and dependence on local volume fraction. *J. Mech. Phys. Solids* 47, 465–502.
- Iyengar, N., Curtin, W.A., 1997. Time-dependent failure in fiber reinforced composites by matrix and interface shear creep. *Acta Mater.* 45, 1489–1502.
- Lagoudas, D.C., Hui, C.Y., Phoenix, S.L., 1989. Time evolution of overstress profiles near broken fibers in a composite with a viscoelastic matrix. *Int. J. Solids Struct.* 25, 45–66.

- Lifshitz, J.M., Rotem, A., 1970. Time dependent longitudinal strength of unidirectional fibrous composites. *Fibre Sci. Technol.* 3, 1–20.
- Melanitis, N., Galiotis, C., Tetlow, P.L., Davies, K.L., 1993. Monitoring the micromechanics of reinforcement in carbon fibre/epoxy resin systems. *J. Mater. Sci.* 28, 1648–1654.
- Miyake, T., Yamakawa, T., Ohno, N., 1998. Measurement of stress relaxation in broken fibers embedded in epoxy using Raman spectroscopy. *J. Mater. Sci.* 33, 5177–5183.
- Ohno, N., Miyake, T., 1999. Stress relaxation in broken fibers in unidirectional composites: modeling and application to creep rupture analysis. *Int. J. Plasticity* 15, 167–189.
- Otani, H., Phoenix, S.L., Petrino, P., 1991. Matrix effects on lifetime statistics for carbon fibre–epoxy microcomposites in creep rupture. *J. Mater. Sci.* 26, 1955–1970.
- Phoenix, S.L., Schwartz, P., Robinson IV, H.H., 1988. Statistics for the strength and lifetime in creep rupture of model carbon/epoxy composites. *Compos. Sci. Technol.* 32, 81–120.
- Schadler, L.S., Galiotis, C., 1995. Review of the fundamentals and applications of laser Raman spectroscopy microprobe strain measurements in composite materials. *Int. Mater. Rev.* 40, 116–134.
- Schadler, L.S., Melanitis, N., Galiotis, C., Figueroa, J.C., Laird, C., 1992. Interphase behavior in carbon/thermoplastic model composites using laser Raman spectroscopy. *J. Mater. Sci.* 27, 1663–1671.
- Schapery, R.A., 1964. Application of thermodynamics to thermomechanical fracture and birefringent phenomena in viscoelastic media. *J. Appl. Phys.* 35, 1451.
- Schapery, R.A., 1967. Stress analysis of viscoelastic composite materials. *J. Compos. Mater.* 1, 228–267.
- Schapery, R.A., Vogt, J.P., Clemmer, L.E., 1967. Report: AA/ES-66-6, AFRPLTR-67-106, 134.
- Schjødt-Thomsen, J., Pryz, R., 2000. Non-linear creep modelling of single-fibre model composites. *Compos. Sci. Technol.* 60, 1791–1800.
- Shanghnessy, G., Snide, J.A., 1984. Preliminary review of statistical treatment of S-glass/epoxy stress rupture data, AFWAL-TR-84-4104, September.
- Thomsen, J.S., Pryz, R., 1999. Creep of carbon/polypropylene model composites—a Raman spectroscopic investigation. *Compos. Sci. Technol.* 59, 1375–1385.
- Zhou, C., Schadler, L.S., Beyerlein, I.J., 2002. Time-dependent micromechanical behavior in graphite/epoxy composites under constant load: a combined experimental and theoretical study. *Acta Mater.* 50, 365–377.